Sound Velocities and Equation of State of iron-rich (Mg,Fe)O

Thesis by

June K. Wicks

In Partial Fulfillment of the Requirements

for the Degree of

Doctor of Philosophy

California Institute of Technology

Pasadena, California

2013

(Submitted)

Acknowledgements

First and foremost, I want to thank my advisor Jennifer Jackson. You've believed in me through this whole process, and pushed me to become a better version of myself. Under your mentorship I've grown both personally and intellectually. I wouldn't be here without you, and looking back I am amazed at how far we've come. I hope that someday I'll become as innovative and well-respected a scientist as you are today. You've been the best role model.

I am thankful to Paul Asimow and George Rossman for your friendship and mentorship, for helping me become a better teacher and a better scientist, and for always having your door open for me, even on weekends and holidays. Thank you George, for letting me hang out in the lab with you for hours at a time just for fun. Thank you Paul, for sharing your wife and kids with me, letting them be such an important part of my life.

Thank you, Mike Gurnis, for taking the time to be on my committee and including me in the CSEDI discussions. Thanks to you and Dan Bower, I could learn about and appreciate first hand the insight from dynamic models of the deep earth. This collaboration has taught me so much and has given me a different perspective on future projects.

I am grateful to Chi Ma, my mentor in the Analytical Facilities. Thanks for letting me putter around to learn the instruments, for letting me teach classes even though it was helping me more than it was helping the students, and for stepping back in and teaching me as well when I was in over my head. Thank you, John Beckett, for teaching me my way around the synthesis lab. Your thoughtful and thorough way of teaching gave me the good habits that I still have today. Thank you, Bin Chen, for the hours in the diamond anvil cell lab, teaching me the tricks you've learned along the way to make the successful cells.

I am so thankful to the great friendships that I have made, to those of you that supported me through this experience: Colette Caggiano, Lauren Edgar (roommate of 4+ years! longest relationship yet!), Melanie Channon, Andrew and Kelly Matzen, Danny and Dani Bower, Emily Hamecher, Aaron Wolf, Mike Baker, Dongzhou Zhang, Jeremy Boyce, and Jed Mosenfelder, and to the members of SSRG and secDEC, you know who you are. Thank you Kevin Lewis and John Bagert, for being my number one fans.

These measurements were made with the help of graduate students Dongzhou Zhang, Aaron Wolf, and Caitlin Murphy, post-doctorate Bin Chen and post-doctorate Hasan Yavas. At the Advanced Photon Source, thank you to my co-authors from GSECARS: Vitali Prakapenka, Kirill Zhuravlev, and Sergey Tkachev. I am particularly grateful to the nuclear resonant and inelastic X-ray scattering group: Jiyong Zhao, Tom Toellner, Ercan Alp, and especially Wolfgang Sturhahn, who has played a large role in my mentorship as well.

Support for this work was provided by the NSF-EAR 0711542 and CAREER EAR-0956166 (both awarded to JMJ) and CSEDI EAR-0855815 (awarded to MCG, DVH and JMJ). The Advanced Light Source is supported by the Director, Office of Science, Office of Basic Energy Sciences(BES), of the U.S. Department of Energy(DOE) under Contract No. DE-AC02-05CH11231. High temperature X-ray diffraction and neon loading was performed at GeoSoilEnviroCARS (Sector 13), Advanced Photon Source (APS), Argonne National Laboratory. GeoSoilEnviroCARS is supported by the National Science Foundation Earth Sciences (EAR-1128799) and Department of Energy Geosciences (DE-FG02-94ER14466). Sector 3 operations, where the nuclear resonant experiments were conducted, are partially supported by COMPRES (NSF EAR 06-49658). Use of the Advanced Photon Source was supported by the U.S. Department of Energy, Office of Science, Office of Basic Energy Sciences, under contract No. DE-AC02-06CH11357. Sample synthesis was carried out in the petrological facilities at Caltech. Microprobe analyses were carried out at the Caltech GPS Division Analytical Facility (funded in part by the MRSEC Program of the NSF under DMR-0080065).

Abstract

Ultralow-velocity zones (ULVZs) are small structures at the base of the mantle characterized by sound velocities up to 30% lower than those of surrounding mantle. In this thesis, we propose that iron-rich (Mg,Fe)O plays a key role in the observed sound velocities, and argue that chemically distinct, iron-enriched structures are consistent with both the low sound velocities and the measured shapes of ULVZs.

We have determined the room temperature Debye sound velocity (V_D) of $(\mathrm{Mg_{0.16}{}^{57}Fe_{0.84}})\mathrm{O}$ up to 121 GPa using nuclear resonant inelastic X-ray scattering. Using an estimate of the equation of state, the seismically relevant compressional (V_P) and shear (V_S) wave velocities were calculated from the V_Ds. We have also determined the room temperature V_D at multiple pressure points of $(\mathrm{Mg_{0.06}{}^{57}Fe_{0.94}})\mathrm{O}$ using nuclear resonant inelastic X-ray scattering and in-situ X-ray diffraction up to 80 GPa. The effect of the electronic environment of the iron sites on the velocities of both of these studies were tracked in-situ using synchrotron Mössbauer spectroscopy. We also present the pressure-volume-temperature equation of state of $(\mathrm{Mg_{0.06}{}^{57}Fe_{0.94}})\mathrm{O}$ determined up to pressures of 120 GPa and temperatures of 2000 K. We combine these studies with a simple Voigt-Reuss-Hill mixing model to predict the properties of a solid ULVZ and show that a small amount of iron-rich (Mg,Fe)O can greatly reduce the average sound velocity of an aggregate assemblage. When combined with a geodynamic model of a solid ULVZ (*Bower et al.*, 2011), we can directly correlate inferred sound velocities to mineralogy and predicted ULVZ shapes. Our combined geodynamic and mineral physics model of a solid ULVZ can be used to explore the relationship between the observed sound velocities and mineralogy of ULVZs with added insight into ULVZ morphology.

Contents

Acknowledgements **iv**

Abstract **vi**

List of Tables **xii**

1 Introduction **2**

1.1 Ultralow-Velocity Zones 2

1.2 Thesis Overview 5

2 Sound velocities of ($Mg_{0.16}Fe_{0.84}$)O measured by Nuclear Resonant Inelastic X-Ray Scattering **6**

2.1 Nuclear Resonant Scattering 6

2.1.1 Nuclear Resonant Inelastic X-Ray Scattering (NRIXS) 7

2.1.2 Synchrotron Mössbauer Spectroscopy (SMS) 8

2.2 Experiments and Data Evaluation 10

2.3 Results 16

2.4 Ultralow-Velocity Zones 18

3 Nuclear Resonant Spectroscopy of ($Mg_{0.06}Fe_{0.94}$)O at high pressure with in-situ X-ray Diffraction **21**

3.1 Introduction 21

3.2 X-ray Diffraction 23

3.3 Experimental Details 25

3.3.1 NRIXS with in-situ XRD 25

3.3.2 SMS with in-situ XRD 26

3.4 Results 27

3.4.1 XRD: Isothermal Equation of State 27

3.4.2 SMS: Magnetic Ordering Transition 29

3.4.3 NRIXS: Sound Velocities 30

4 Thermal Equation of State of ($Mg_{0.06}Fe_{0.94}$)O 41

4.1 Introduction 41

4.2 Previous Studies 41

4.3 Experimental Details 42

4.4 Results 44

4.4.1 Phase Identification 44

4.4.2 Equations of State 47

4.5 Discussion 51

4.5.1 Effect of Buffering on Equation of State 51

4.5.2 Effect of Composition on the Thermal Equation of State of (Mg,Fe)O 54

4.6 Rhombohedral Distortion of ($Mg_{0.06}Fe_{0.94}$)O 56

5 Implications for Ultralow-velocity Zones 61

5.1 Physical Mixing Models 61

5.1.1 Extrapolation of Magnesiowüstite properties to the CMB 61

5.1.2 Mixture of Magnesiowüstite and Ambient Mantle 63

5.1.3 Mixture of Magnesiowüstite and Silicate Perovskite 64

5.1.4 Dynamics of a Solid-state ULVZ 66

5.2 Conclusions 69

Bibliography 70

A **82**

A.1 Synthesis and Characterization 82

A.1.1 $(Mg_{0.16}Fe_{0.84})O$ 82

A.1.2 $(Mg_{0.06}Fe_{0.94})O$ 83

A.1.3 $Fe_{1-x}O$ 83

A.2 Additional Thermodynamic Parameters 84

A.2.1 $(Mg_{0.16}Fe_{0.84})O$ 84

A.2.2 $(Mg_{0.06}Fe_{0.94})O$ 85

A.3 Sound Velocities of FeO from Nuclear Resonant Inelastic X-ray Scattering 86

List of Figures

1.1 Modal Mineralogy of the Earth's Mantle 3

2.1 Setup of Nuclear Resonant Scattering measurements at Sector 3-ID-B of the Advanced Photon Source (APS) 7

2.2 Sample NRIXS spectrum of $(Mg_{.06}Fe_{.94})O$ 8

2.3 Sample Mössbauer spectra of $(Mg_{.06}Fe_{.94})O$ 9

2.4 Energy scans (raw NRIXS spectra) of $(Mg_{.16}Fe_{.84})O$ at 300 K over 0 to 120 GPa . . . 11

2.5 Partial projected phonon density of states (PDOSs) of $(Mg_{.16}Fe_{.84})O$. 12

2.6 Time spectra of $(Mg_{.16}Fe_{.84})O$ from synchrotron Mössbauer spectroscopy. 13

2.7 Determination of the Debye sound velocity of $(Mg_{.15}Fe_{.85})O$ at 0 and 121 GPa. 14

2.8 Debye sound velocities of $(Mg_{.16}Fe_{.84})O$ (this study) and of $Fe_{.947}O$ (*Struzhkin et al.*, 2001) at 300 K. 15

2.9 V_P and V_S of $(Mg_{.16}Fe_{.84})O$ determined from V_D compared to PREM and ULVZs . . 16

2.10 Voigt-Reuss-Hill (VRH) mixing of V_P, V_S, and density of $(Mg_{.16}Fe_{.84})O$ with PREM . 19

3.1 Cubic to rhombohedral transition pressures in the literature 22

3.2 Illustration of Bragg's law in X-ray diffraction 24

3.3 $(Mg_{0.06}Fe_{0.94})O$ loaded for SMS study 26

3.4 Pressure-volume data of $(Mg_{0.06}Fe_{0.94})O$ at 300 K, measured in the SMS study 28

3.5 Pressure-Volume equation of state of $(Mg_{0.06}Fe_{0.94})O$ at 300 K 30

3.6 Synchrotron Mössbauer spectra of $(Mg_{0.06}Fe_{0.94})O$ at 300 K 31

3.7 In-situ synchrotron Mössbauer spectra of $(Mg_{0.06}Fe_{0.94})O$ at 300 K 32

3.8 Raw NRIXS spectra of $(Mg_{0.06}Fe_{0.94})O$ at 300 K 33

3.9 PDOSs of $(Mg_{0.06}Fe_{0.94})O$ at 300 K 34

3.10 Debye velocity determination using *psvl* 35

3.11 Debye velocity (V_D) of $(Mg_{0.06}Fe_{0.94})O$ at 300 K 37

3.12 V_D of $(Mg_{0.06}Fe_{0.94})O$ compared to FeO and $(Mg_{0.65}Fe_{0.35})O$ at 300 K, as a function of density 38

3.13 Compressional (V_P) and shear (V_S) wave velocities of $(Mg_{0.06}Fe_{0.94})O$ at 300 K 39

4.1 Example XRD spectra at 85 GPa showing peak identifications for *B*2-NaCl, *hcp*-Fe, Ne, and $(Mg_{0.06}Fe_{0.94})O$. 43

4.2 Phase identification of $(Mg_{0.06}Fe_{0.94})O$ in P–T space. 48

4.3 P-V-T data and isotherms of *B*1-structured $(Mg_{0.06}Fe_{0.94})O$ in the buffered experiment 50

4.4 P-V-T data and isotherms of *B*1-structured $(Mg_{0.06}Fe_{0.94})O$ in the unbuffered experiment 52

4.5 Overlay of data and equations of state of buffered and unbuffered $(Mg_{0.06}Fe_{0.94})O$ . . 53

4.6 Comparison of volume measurements and equations of state of $(Mg_{0.06}Fe_{0.94})O$ to *B*1-FeO. 54

4.7 Thermal expansion of buffered $(Mg_{0.06}Fe_{0.94})O$ at 1900 K as a function of pressure, compared to FeO, $(Mg_{0.64}Fe_{0.36})O$ and MgO. 55

4.8 Evolution of d-spacings of $(Mg_{0.06}Fe_{0.94})O$ as a function of pressure 57

4.9 Evolution of c/a ratios of rhombohedral $(Mg_{0.06}Fe_{0.94})O$ as a function of pressure at 300 K 58

4.10 Pressure-volume data of quenched, rhombohedral $(Mg_{0.06}Fe_{0.94})O$ at 300 K 59

5.1 Debye velocity as a function of density of $(Mg_{.16}Fe_{.84})O$, $(Mg_{.06}Fe_{.94})O$, and FeO . . 62

5.2 Mixing models: V_P, V_S, and density of $(Mg_{.16}Fe_{.84})O$+PREM 64

5.3 Mixing models: V_P, V_S, and density of $(Mg_{.16}Fe_{.84})O$+Pv 66

5.4 Dynamic model interpretation of mixing models at 4000 K 68

A.1 Secondary electron image of $(Mg_{0.06}Fe_{0.94})O$ 83

A.2 NRIXS spectra of FeO 87

A.3 PDOS of FeO 88

List of Tables

1.1 Summary of experiments presented in this thesis 5

2.1 Summary of pressure, density, Debye sound velocity (V_D), and compressional (V_P) and shear (V_S) wave speeds of $(\mathrm{Mg}_{.16}\mathrm{Fe}_{.84})\mathrm{O}$. 17

3.1 Details of the $(\mathrm{Mg}_{0.06}\mathrm{Fe}_{0.94})\mathrm{O}$ NRIXS experiment 26

3.2 XRD results of the $(\mathrm{Mg}_{0.06}\mathrm{Fe}_{0.94})\mathrm{O}$ SMS experiment 27

3.3 Equations of state fit to the $(\mathrm{Mg}_{0.06}\mathrm{Fe}_{0.94})\mathrm{O}$ dataset. 29

3.4 Debye Velocity (V_D) of $(\mathrm{Mg}_{0.06}\mathrm{Fe}_{0.94})\mathrm{O}$ as a function of in-situ density 36

3.5 Summary of sound velocities of $(\mathrm{Mg}_{0.06}\mathrm{Fe}_{0.94})\mathrm{O}$ as a function of pressure 40

4.1 Pressure-volume-temperature data for the buffered experiment 45

4.2 Pressure-volume-temperature data for the unbuffered experiment 46

4.3 3rd-order Birch-Murnaghan equation of state parameters for the buffered dataset using *hcp*-Fe as a pressure marker. 49

4.4 3rd-order Birch-Murnahan equation of state parameters the both the buffered and unbuffered dataset using $B2$-NaCl as a pressure marker 50

4.5 Equation of state parameters using $B2$-NaCl as a pressure marker, with K_{0T} fixed to 180 GPa. 51

4.6 Pressure-volume data for the buffered experiment at 300 K. 60

5.1 Model parameters for mixing model “Mw+PREM” 64

5.2 Model parameters for mixing model “Mw+Pv” 66

5.3 Model parameters for mixing model “Mw+PREM” and “Mw+Pv” at 4000 K 68

A.1 Thermodynamic parameters calculated directly from the PDOS of $(Mg_{0.16}Fe_{0.84})O$. . 84

A.2 Thermodynamic parameters calculated directly from the PDOS of $(Mg_{0.06}Fe_{0.94})O$ . . 85

A.3 Summary of FeO density and Debye Velocities 86

Chapter 1

Introduction

Study of the interior of the earth is crucial to understanding both the processes by which a planet was formed and the future impact of deep interior dynamics.

Much has been learned from seismic studies, probing the propagation of sound waves through the earth. Seismic reflectors deep in the earth such as those located at 410, 660 and 2900 km below the earth's surface have been interpreted as chemical boundaries or phase changes, supported by experimental studies of model compositions of primitive mantle material. The major discontinuities in the mantle are believed to correspond to phase changes, where olivine transforms to the high pressure polymorph wadsleyite at the 410 km discontinuity, then breaks down to form ferropericlase and perovskite at the 660 discontinuity (e.g. *Irifune*, 1994, Figure 1.1).

The mantle layer between the core-mantle boundary and the D" discontinuity spans a depth range in Earth's lower mantle from up to 350 km above the liquid outer core to the outer core itself, corresponding to a proposed temperature range of 3300-4300 K and 115 to 135 GPa. Intermittent detection of this discontinuity suggests that the core-mantle boundary (CMB) layer is compositionally distinct and/or represents a different phase assemblage (e.g. *Lay et al.*, 2008; *Sidorin et al.*, 1999).

1.1 Ultralow-Velocity Zones

At the base of the D" layer, 5-20 km thick patches have been observed in which the V_P and V_S sound velocities are reduced by 5-10% and 10-30% (*Thorne and Garnero*, 2004). Reduced seismic

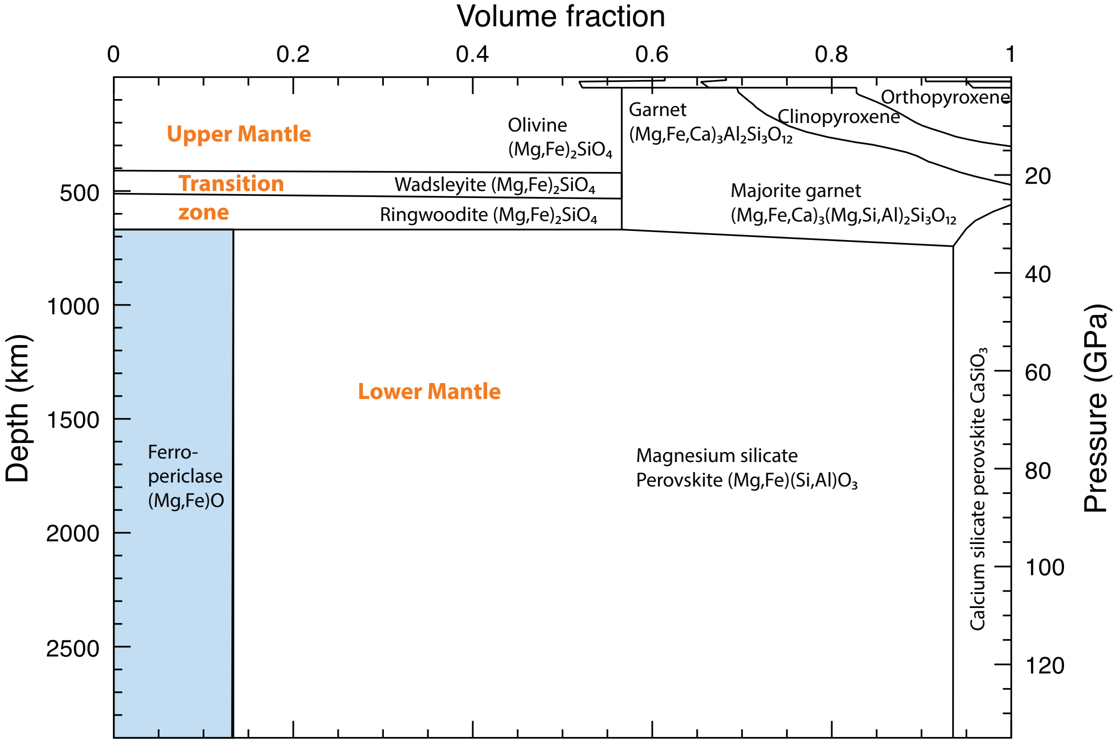

Figure 1.1: Modal mineralogy of the earth's mantle, assuming a pyrolite mantle. The upper mantle (0-440 km below the earth's surface) is mostly comprised of olivine garnet, and pyroxenes $(Mg,Fe)_2Si_2O_6$. The lower mantle (660 to 2900 km below the earth's surface) is comprised of Ca- and (Mg,Fe)- silicate perovskite and (Mg,Fe)O. Highlighted in blue is ferropericlase, the Fe-poor member of the MgO-FeO solid solution. Iron-rich members are named magnesiowüstite. Figure is adapted from (*Frost et al.*, 2004)

velocities in this ultra-low velocity zone, or ULVZ, were first attributed to partial melting due to drastic velocity reductions, sharp upper boundaries, and a strong correlation with hot spots on the surface (e.g. *Williams and Garnero*, 1996; *Williams et al.*, 1998; *Lay et al.*, 2004). A sound velocity decrement ratio $\partial V_P/\partial V_S$ of 1:3 has been shown to be consistent with partial melt (*Berryman*, 2000).

Numerous seismic studies of the core-mantle boundary indicate that ULVZ distribution is patchy and sometimes associated with edges or the interior of large low shear velocity provinces (*McNamara et al.*, 2010). Fine-scale one-dimensional structure of some ULVZs have been probed, finding a steep positive velocity gradient with depth, implying complex interior morphology (*Rost et al.*, 2006). Multiple concave-down ULVZs clustered together have been invoked to explain PKP precursors in a two-dimensional study, giving the first seismic insight into ULVZ shape (*Wen and Helmberger*, 1998).

Partial melting of ambient mantle would require the fortuitous intersection of the mantle solidus with the base of the core-mantle boundary. Recent work into the equations of state of fayalite Fe_2SiO_4 liquid and subsequent analysis shows that partial melting of chondrite or peridotite liquid is unlikely to be gravitationally stable at the base of the mantle (*Thomas et al.*, 2012). It has been proposed that enriched residues of a crystallizing mantle could be depleted in Si and enriched in FeO enough to form ULVZs (*Labrosse et al.*, 2007; *Nomura et al.*, 2011).

Dynamic studies exploring the stability of partially-molten ULVZs show that the amounts of liquid required to reduce the velocities of an assemblage would percolate and pool at the base of the mantle rather than remain suspended in a ULVZ (*Hernlund and Tackley*, 2007). Partial melt can be maintained km's above the CMB if the ULVZ is stirred (*Hernlund and Jellinek*, 2010). Further studies of melt geometry explore mechanisms to retain greater melt fraction (*Wimert and Hier-Majumder*, 2012; *Hier-Majumder and Abbott*, 2010, e.g.). In the end, a seemingly simple explanation is complicated by large unknowns in grain boundary properties, melt viscosity, and melt sound velocities.

Solid ULVZs have also been considered in the literature, in the form of FeO/FeSi alloy (*Manga and Jeanloz*, 1996) or iron-enriched post-perovskite (*Mao et al.*, 2006), but are no longer considered stable in the hot core-mantle boundary regions in which ULVZs are found. In this thesis, we introduce and explore another alternative: iron-rich (Mg,Fe)O.

The partitioning behavior of iron between perovskite(Pv), post-perovskite(PPv), and (Mg,Fe)O varies widely based on experimental conditions. Recently, it has been suggested that iron preferentially partitions in (Mg,Fe)O in the presence of Pv and PPv based on analyses of quenched phase assemblages from pressures and temperatures of 100 GPa and ~1800 K (*Auzende et al.*, 2008; *Sinmyo et al.*, 2008). An enhanced iron content and subsequent uptake by (Mg,Fe)O could result in a composition much more iron-rich than previously considered. Therefore, it is of interest to study the elasticity of iron-rich (Mg,Fe)O at core-mantle boundary conditions, as it may shed light on seismic observations in this region.

1.2 Thesis Overview

This thesis is divided into three studies of iron-rich oxide, the experiments for which are summarized in Table 1.1. All of these studies are united by the use of X-ray scattering techniques using synchrotron radiation to measure the elasticity of iron-rich (Mg,Fe)O. We synthesized our own samples for this study, and describe the samples in Section A.1. Using a diamond anvil cell to create pressures approaching those of the core-mantle boundary and occasionally in-situ laser heating to create temperatures approaching those of the earth's interior, we measured material properties relevant to the study of the earth's mantle, namely sound velocities and densities.

Chapter 2 is a study of $(Mg_{.16}Fe_{.84})O$ using nuclear resonant inelastic X-Ray scattering (NRIXS) and synchrotron Mössbauer spectroscopy (SMS). Chapter 3 measured the sound velocities and magnetic state of $(Mg_{.06}Fe_{.94})O$ using the methods described in Chapter 2 with a few key differences, including the use of in-situ X-ray diffraction to measure lattice spacing of the sample and map it directly to a combined XRD/SMS study of the same material. Chapter 4 describes the P-V-T equation of state of $(Mg_{.06}Fe_{.94})O$. Finally, we close in Chapter 5 with a mixing model that combines the results of our work with dynamic calculations of a solid ULVZ.

Chapter	beamlines	beamtime dates	information collected	P-T conditions	samples
2	APS 3-ID-B	10/08, 7/09	NRIXS, in-situ SMS	300 K, 0-121 GPa	Mw84
	ALS 12.2.2	4/09	XRD	300 K, 0 GPa	Mw84
3	APS 3-ID-B	8/11, 10/12	NRIXS, in-situ SMS	300 K, 0-81 GPa	Mw94
	APS 3-ID-B	2/13	SMS with in-situ XRD	300 K, 8-52 GPa	Mw94
4	APS 13-ID-D	7/11	XRD	300-1950 K, 32-120 GPa	Mw94
	APS 13-ID-D	2/12	XRD with Fe buffer	300-1800 K, 30-70 GPa	Mw94
A.3	APS 3-ID-B	8/11, 3/12	NRIXS	300 K, 0-100 GPa	FeO
	ALS 12.2.2	5/11	XRD	300 K, 0 GPa	FeO
	APS 13-ID-D	2/12	XRD	300 K, 100 GPa	FeO

Table 1.1: Summary of experiments presented in this thesis